RESEARCH ARTICLE

Journal *American Ceramic Society*

The catalytic activity of the $Pr_2Zr_{2-x}Fe_xO_{7\pm\delta}$ system for the CO oxidation reaction

Emerson Luiz dos Santos Veiga[1] ⓘ | Xavier Vendrell Villafruela[2] ⓘ | Jordi Llorca[2] | Hector Beltrán-Mir[1] ⓘ | Eloísa Cordoncillo[1]

[1]Departamento de Química Inorgánica y Orgánica, Universitat Jaume I de Castellón, Castellón de la Plana, Spain

[2]Institute of Energy Technologies, Department of Chemical Engineering and Barcelona Research Center in Multiscale Science and Engineering, Universitat Politècnica de Catalunya, Barcelona, Spain

Correspondence
Hector Beltrán-Mir and Eloísa Cordoncillo, Departamento de Química Inorgánica y Orgánica, Universitat Jaume I de Castellón, Av. Sos Baynat s/n, Castellón de la Plana 12071, Spain.
Email: mir@uji.es and cordonci@uji.es

Abstract

One of the alternatives to decrease the concentration of CO is its oxidation reaction to CO_2, which can be made more efficient using catalysts. In this work, it is shown that pyrochlore structures are a promising candidate to act as heterogeneous catalysts due to their chemical and physical properties. For use as a catalyst in this reaction, the $Pr_2Zr_{2-x}Fe_xO_{7\pm\delta}$ ($x = 0$, 0.05, 0.10, and 0.15) system was synthesized by the solvothermal method, firing the powder obtained at temperatures of 1200 and 1400°C. The diffraction patterns confirmed the pyrochlore structure as the single phase in all the nominal compositions. The Brunauer–Emmett–Teller method and dynamic light-scattering analysis showed an increase in the particle size and a decrease in the specific surface area when increasing the iron concentration and increasing the calcination temperature. The compositions that presented the best catalytic activity were the samples with the highest iron concentration. Moreover, these samples were able to convert all the CO oxidation reactions in a narrower temperature range than a conventional CeO_2 sample. The presence of vacancies and the redox behavior of the elements present are the key factors for the catalysis of this system in the CO oxidation reaction.

KEYWORDS
CO oxidation reaction, heterogeneous catalysis, oxidation state, praseodymium and iron, pyrochlore

1 | INTRODUCTION

Due to population growth and the consequent increase in consumerism, there is a rising concern about the energy demand required to sustain the functioning of all the different sectors of society. Hence, there is an important ongoing debate about how to deal with the imminent climate change, because the attempts to

implement renewable energy sources are not yet sufficient to cover today's need to use fossil fuels.[1–3] Although goals are being set by political organizations with the participation of most countries,[4,5] the current scenario indicates that humanity will have to live for a few more decades with the problems generated by the combustion of fossil fuels, such as respiratory diseases, and emissions of toxic gases like sulfur dioxide and nitrogen oxides, besides high concentrations of carbon monoxide and dioxide in the atmosphere.[6]

In particular, carbon monoxide (CO), which comes from the incomplete combustion of fossil fuels, is one of the most toxic gases to human health, where exposure to this gas can lead to asphyxiation as well as cardiovascular and respiratory problems.[7–11] To reduce the concentration of CO in the atmosphere, its conversion to carbon dioxide (CO_2) through catalytic oxidation processes emerges as a more environmentally friendly alternative. To carry out the CO oxidation reaction, different strategies have been studied, the vast majority of which use an inorganic structure decorated with noble metals such as Pd, Pt, and Rh.[12–19]

Among the most studied materials, cerium dioxide (CeO_2) stands out because of its excellent physicochemical properties, oxygen exchange capability, the possible creation of oxygen vacancies, and its redox characteristics. The application of ceria-based materials is determined by the electronic configuration of cerium and the high stability of its two valence states. The reduction of Ce^{4+} to Ce^{3+} is accompanied by a loss of oxygen and, hence, the formation of oxygen vacancies. The conversion between the two oxidation states is the key process that determines the ability of cerium oxide to release or adsorb oxygen. CeO_2 is capable of storing oxygen under combustion conditions and can release oxygen when exposed to reducing agents.[20–24] Thus, the oxygen vacancies are an essential point to achieve high catalytic performance in oxidation reactions. Depending on the reaction conditions, pure CeO_2 can fully convert CO into CO_2 in the temperature range between 250 and 400°C.[25–28] Other materials used as catalysts for this reaction are shown in Table S1.

As an alternative to CeO_2, pyrochlore-type structures, with the general formula $A_2B_2O_7$, appear as promising candidates to promote atmospheric depollution through catalytic reactions. The outstanding features of pyrochlore, like good thermal stability, oxygen mobility, inherent oxygen vacancy, and good ionic transport, make this structure suitable for use in several areas, such as the manufacture of fuel cells,[29–32] in the production of hydrogen,[33] as gas sensors,[34,35] as a thermal barrier coating,[36,37] and for photocatalysis.[38] Recently, pyrochlore structures have been studied for soot oxidation,[39] ammonia oxidation,[40] methane dry reforming,[41] electrocatalysis,[42,43] and photocatalysis.[44]

The stable crystalline phase for pyrochlore-type structures has already been unveiled by previous literature[45–47] and depends on the ratio between the ionic radius of the atoms located on sites A and B. An ordered pyrochlore phase with space group *Fd*-3*m* will be formed when the rA/rB ratio is in the range of 1.46 and 1.78. In this case, site A is usually occupied by an ion with oxidation numbers +2 or +3, such as La, Pr, Sm, Ca, and Sr, among others, and they are surrounded by eight oxygen ions. On the other hand, the B-site is usually occupied by transition metals, such as Zr, Ti, or Nb, with oxidation states +4 or +5, and they are sixfold coordinated with oxygens.[45]

It is expected that pyrochlore structures with elements with multiple valence states, such as Pr, Eu, Tb, and Yb, are more active for catalytic reactions than those with elements presenting a single valence state. This characteristic is due to the ease of oxygen exchange between the catalyst and the gas phase when more than one valence state is present.[45] In our previous work,[48] it was demonstrated that in a pyrochlore with the formula $Pr_2Zr_{2-x}Fe_xO_{7\pm\delta}$ ($x = 0$, 0.05, and 0.10) synthesized by the coprecipitation method, the presence of oxygen vacancies together with the redox characteristics of the ions present were able to retain oxygen in the structure, depending on the atmosphere and temperature. After these initial investigations, this work aims to evaluate the capacity of this material to perform as a heterogeneous catalyst for the CO oxidation reaction.

2 | EXPERIMENTAL SECTION

2.1 | Synthesis method

Four different nominal compositions of the $Pr_2Zr_{2-x}Fe_xO_{7\pm\delta}$ ($x = 0$, 0.05, 0.10, and 0.15) system were prepared by the solvothermal method. This synthesis method, as well as other chemical synthesis approaches, has advantages over the traditional ceramic method, for example, it requires lower temperatures to obtain the material, it is possible to obtain nano-sized particles, it is relatively simple and economical, it has better control of the reaction stoichiometry, and the synthesis is more easily reproducible.[49] The reagents used were $Pr(CH_3COO)_3 \cdot XH_2O$ (Strem Chemicals, 99.9%), $ZrOCl_2 \cdot 8H_2O$ (Alfa Aesar, 98%), and $Fe(NO_3)_3 \cdot 9H_2O$ (Strem Chemicals, 98%). The zirconium, praseodymium, and iron precursors were dissolved in 25 ml of a 2.5 mol L^{-1} solution of HNO_3 (Labkem, 65%), and then the pH of the solution was adjusted to seven using ammonia solution (Scharlab, 32% w/w). The suspension thus formed was

stirred vigorously for 10 min and transferred to a Teflon-lined vessel (with 125 ml volume capacity) together with 40 ml of a 3 mol L^{-1} solution of KOH (Labkem, 85%) used as a catalyst. The total volume of the solution also containing the catalyst was ~80 ml. The Teflon vessel was placed in an autoclave and heated in an oven at 180°C for 24 h. Then the system was cooled, and the suspension was centrifuged for 8 min at 11000 rpm, washed with distilled water and ethanol, and dried at 100°C for 24 h.

The powders resulting from the compositions thus prepared were calcined at two different temperatures, 1200 and 1400°C, for 2 h with a heating ramp of 5°C min^{-1}.

Each nominal composition was referenced according to its iron concentration and calcination temperature. For the different compositions, the prefixes PZ0, PZF05, PZF10, and PZF15 were used for the x values of 0, 0.05, 0.10, and 0.15, respectively. The samples calcined at 1200°C received the number "1200," and the samples calcined at 1400°C were given the number "1400."

2.2 | Structural characterization

X-ray diffraction (XRD) analysis was performed using a Bruker-AX D8 ADVANCE X-ray diffractometer with Cu-K_α radiation. All data were collected in the range of $10° \leq 2\theta \leq 70°$ at room temperature with a step size of 0.03° and a counting time of 1 s in each step.

Raman spectra of the different nominal compositions were recorded in the frequency range of 200–700 cm^{-1}. The Raman spectra of the different compositions were acquired on a modular Raman system from WITec GmbH, equipped with an automatic vertical confocal microscope, model alpha300 apyron, with an EMCCD ultrahigh efficiency detector refrigerated at −60°C and with the 532 nm Ar laser line as the excitation source.

Using Micromeritics Gemini V equipment, the specific surface area and pore size analyses were performed under a liquid nitrogen bath using the Brunauer–Emmett–Teller (BET) and Barrett–Joyner–Halenda (BJH) methods, respectively. Prior to analysis, each sample was degassed using N$_2$ for 3 h at 150°C.

Particle dispersions were characterized in aqueous suspension using a dynamic light-scattering (DLS) system (Zetasizer Nano ZS, Malvern Instruments Ltd., Malvern, UK). Specimens of each composition were dissolved in distilled water (0.02 µg ml^{-1}) and measured by DLS. This concentration was used to reach a polydispersity index lower than 0.7. Laser light is dispersed at varying intensities depending on the particle size due to the Brownian motion of particles in suspension. Using the Stokes–Einstein relation, these intensity oscillations are used to calculate the Brownian motion velocity and thus the particle size. A 90° scattering angle and a green laser light (532 nm) were used in the tests.

The microstructure and morphology of the samples were analyzed using a field-emission scanning electron microscope (FE-SEM) JEOL 7001F, with an acceleration voltage of 15 kV. The samples were deposited on an aluminum holder and coated with platinum. The particle size distributions were estimated using ImageJ software.

X-ray photoelectron spectroscopy (XPS) measurements were carried out in a SPECS (SPECS GmbH., Berlin, Germany) system equipped with an XR50 source operated with the Al anode at 150 W, and a Phoibos MCD-9 detector. Binding energy shifts caused by surface charging were corrected by aligning the adventitious carbon component in the C 1s region at 284.8 eV. The XPS data were analyzed with the CasaXPS software. All curves were deconvolved using a 50% Gaussian/50 Lorentzian function, with the ratio between the peaks fixed according to the degeneracy of each spin state. To obtain a proper fitting of the curves, Shirley and Tougaard background were used, with the application of area and FWHM constraints.

2.3 | Catalytic activity

The catalytic behavior of the compositions in the CO oxidation reaction was analyzed using an Agilent 490 Micro Gas Chromatograph equipped with MS 5 Å, Plot U, and Stabilwax Capillary Columns, and TCD detectors were used to measure online gas concentrations every 6–7 min approximately. The crushed catalyst (0.1 g) was diluted with SiC and positioned in the center of a stainless-steel reactor with a quartz wool bed (GHSV 6000 h^{-1}). The reactor was placed inside a vertical furnace connected to an external thermal control system (±0.1°C). Gases were provided by Bronkhorst mass flow controllers. Temperature-dependent catalytic activity tests were performed with a total gas flow of 80 ml min^{-1} and a N$_2$:O$_2$:CO ratio of 23:1:1 (molar basis) between 40 and 500°C (heating ramp of 2°C min^{-1}). The product of the reaction was CO$_2$, and the remaining CO and O$_2$ reactants were also measured. The CO conversion (χCO) was calculated using in the following equation:

$$\chi CO(\%) = \frac{n_{CO,\,in} - n_{CO,\,out}}{n_{CO,\,in}} \cdot 100 = \frac{n_{CO_2,\,out}}{n_{CO,\,in}} \cdot 100 \quad (1)$$

where $n_{CO,\,in}$ is the inlet molar flowrate of CO, $n_{CO,\,out}$ is the outlet molar flowrate of CO that has not reacted, and $n_{CO_2,\,out}$ is the outlet molar flowrate of the CO$_2$ produced during the experiment.

Stability tests were carried out at 300°C under the same gas mixture used in the temperature-dependent catalytic activity experiment, with gas concentration measurements
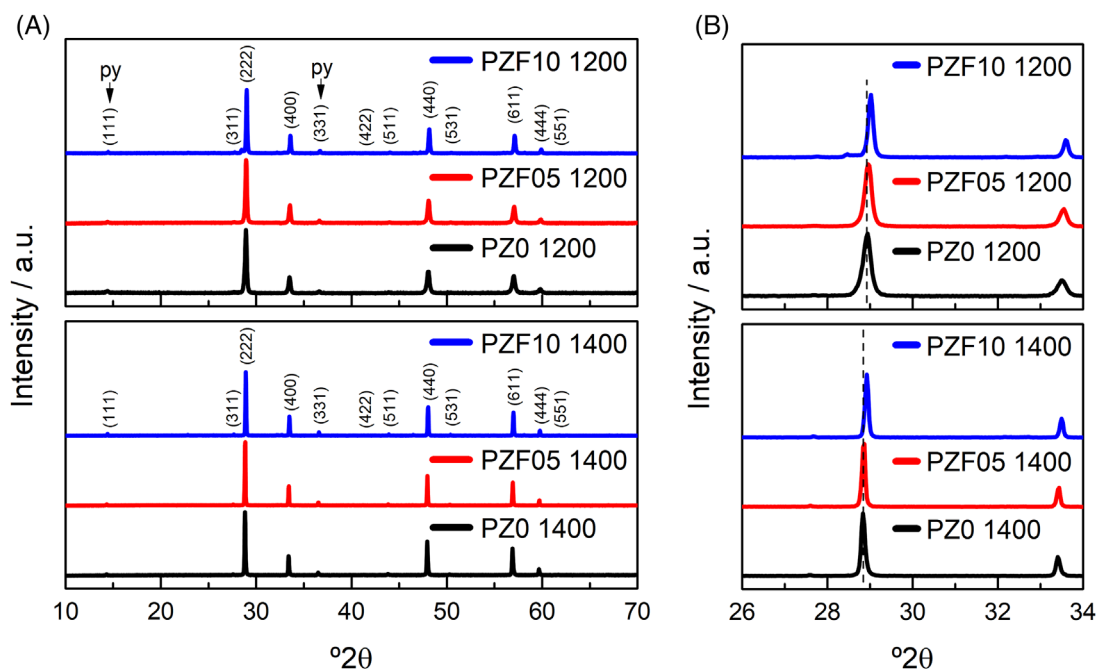
FIGURE 1 (A) X-ray diffraction (XRD) patterns for the $Pr_2Zr_{2-x}Fe_xO_{7\pm\delta}$ system ($x = 0.00, 0.05$, and 0.10) of powders calcined at 1200 and 1400°C for 2 h; (B) the (222) diffraction peak of the pyrochlore phase for all compositions

every 15 min, for 160 h. The CO conversion was calculated using Equation (1).

3 | RESULTS AND DISCUSSION

The calcined powders were grounded and characterized by XRD. All diffractograms are shown in Figure 1A and Figure S1.

For all nominal compositions with $x \leq 0.1$, a single-phase pyrochlore structure (JCPDS-ICDD 19-1021, Fd-$3m$ space group) was identified at both calcination temperatures. The composition with higher iron concentration presented a secondary phase as shown in Figure S1; therefore, this composition was not used for the following studies. The presence of the superstructure peaks at°$2\theta \approx 14°$ (1 1 1) and $37°$ (3 3 1) distinguishes the pyrochlore structure from the defective fluorite structure. These peaks appear due to differences in the radiation scattering of the cations at the A and B sites, the displacement of oxygen from the ideal position, and the distribution of oxygen vacancies.[50] In the iron-doped compositions, there is a peak displacement toward higher 2θ angles compared to the undoped samples (Figure 1B), which indicates a contraction of the unit cell according to Bragg's Law. This contraction is due to three different factors: the substitution of Zr^{4+} ions ($r = 72$ pm, coordination number CN = 6) by Fe^{3+} ions ($r = 55$ pm, CN = 6), the partial conversion of Pr^{3+} ($r = 112.6$ pm, CN = 8) to Pr^{4+} ($r = 96$ pm, CN = 8), and the

presence of nonstoichiometric O^{2-} ions.[51,52] The presence of the ordered pyrochlore structure was also confirmed by Raman spectroscopy, as can be seen in Figure S2.

To investigate the physical properties of the synthesized catalysts, the multipoint BET method and the BJH treatment were used. Table 1 summarizes the specific surface area (S_{BET}) and the mean pore diameter of the nominal compositions that were prepared. The data found indicate a dependence of these properties on both iron concentration and calcination temperature. As the Fe content increases, there is a decrease in surface area. The values found for the surface area also decrease on raising the firing temperature from 1200 to 1400°C.

The PZ0 1200 sample has the maximum specific surface area (8.14 ± 0.02 m^2 g^{-1}), which is reduced as the iron concentration increases. This behavior has already been observed in other studies and is related to a more intense sintering tendency in iron-rich samples compared to undoped compositions.[53,54] The significant reduction of the surface area in the samples calcined at 1400°C is also due to the enhancement of the sintering process at higher temperatures. The average pore diameter found in all compositions did not show any significant variation, and the values are classified as nanopores according to the International Union of Pure and Applied Chemistry classification.[55]

The tendency observed by the BET method is also supported by DLS analysis. The average particle size values found by DLS evidence the tendency to increase the

TABLE 1 Surface area and pore diameter values determined by the Brunauer–Emmett–Teller (BET) and Barrett–Joyner–Halenda (BJH) methods, respectively

Reference	BET Surface area (m²/g)	BJH Pore diameter (Å)	DLS Average diameter (nm)	SEM Average diameter (nm)
PZ0 1200	8.14 ± 0.02	19.7	311	155
PZF05 1200	6.51 ± 0.01	20.7	392	173
PZF10 1200	4.81 ± 0.03	20.5	438	199
PZ0 1400	1.58 ± 0.01	19.6	676	276
PZF05 1400	0.98 ± 0.03	19.3	728	461
PZF10 1400	0.71 ± 0.03	19.8	815	515

Abbreviations: BET, Brunauer–Emmett–Teller; BJH, Barrett–Joyner–Halenda; SEM, scanning electron microscope.

Note: Particle size calculated by the dynamic light scattering (DLS) analysis.
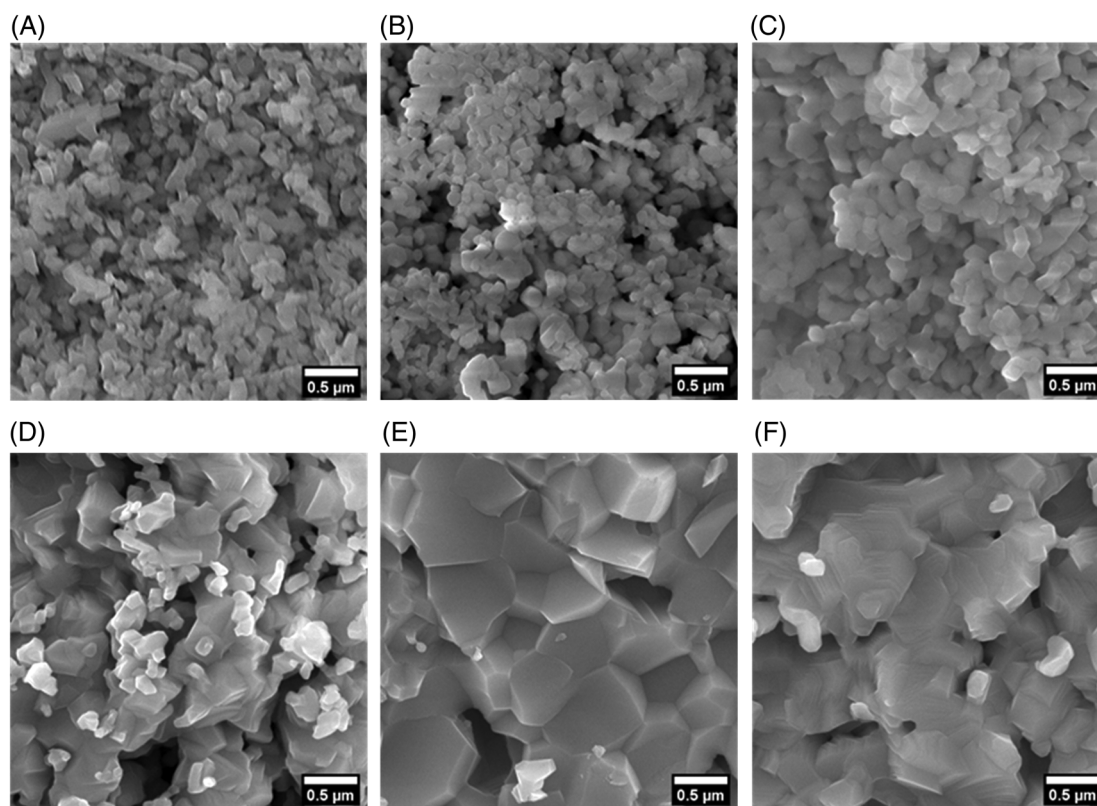
FIGURE 2 Micrographs of the (A) PZ0 1200, (B) PZF05 1200, (C) PZF10 1200, (D) PZ0 1400, (E) PZF05 1400, and (F) PZF10 1400 samples

particle size when increasing the iron concentration from $x = 0$ to 0.10, and also when increasing the calcination temperature from 1200 to 1400°C. Of the two effects that cause the increase in average particle size, the calcining temperature is the one that affects the most.

Comparing the micrographs obtained by SEM presented in Figure 2, growth in particle size is noticed on increasing the iron concentration, maintaining a rounded morphology at a calcination temperature of 1200°C for the three compositions. By increasing the calcination temperature to 1400°C, significant signs of sintering are observed, where

the rounded shape of the particles is practically lost due to the temperature effect. The particle size distribution calculated from the SEM micrographs is available in Figure S3. The differences between the values calculated by the SEM micrographs and those obtained by DLS (Table 1) may be due to possible agglomerated particles when dispersing the powder for DLS analysis. However, despite the differences in the values, the same tendency of increase in particle size is observed in both characterization techniques, showing a dependence of the physical properties on the iron content as well as on the calcination temperature.
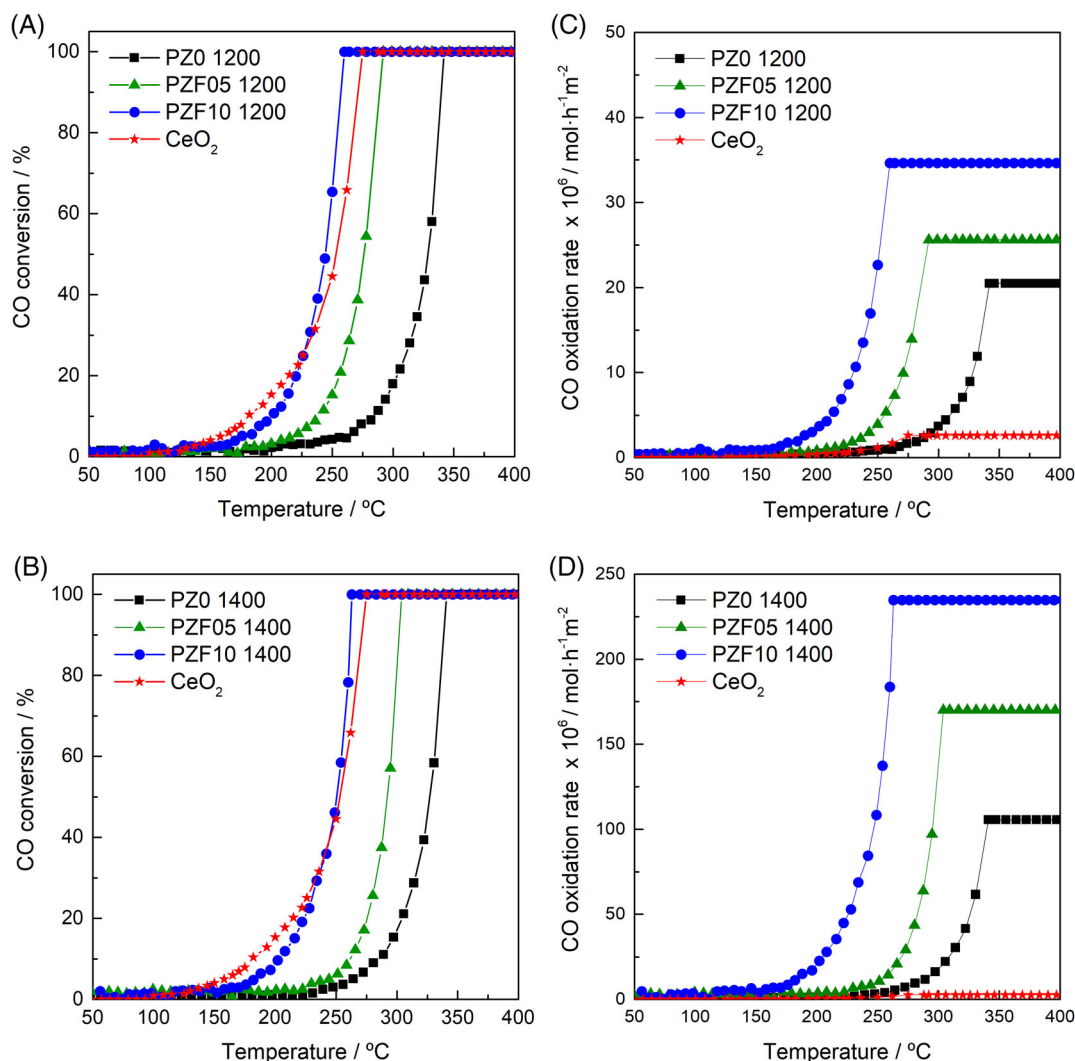
FIGURE 3 Catalytic performance on the CO oxidation reaction of the compositions calcined at (A) 1200°C and (B) 1400°C compared to a CeO_2 sample. CO oxidation rate normalized by Brunauer–Emmett–Teller (BET)-specific surface area as a function of temperature for the compositions calcined at (C) 1200°C and (D) 1400°C

As found in a previous study,[48] the $Pr_2Zr_{2-x}Fe_xO_{7\pm\delta}$ ($x = 0$, 0.05, and 0.10) system contains oxygen vacancies that can be generated by Fe substitution in the position of Zr and by redox processes involving the Pr^{3+}/Pr^{4+} and Fe^{2+}/Fe^{3+} species, in addition to the role of inherent vacancies of the pyrochlore structures. Due to these characteristics, this material could act in a similar way to CeO_2 for the CO oxidation reaction.

The results of the catalytic activity for CO oxidation are shown in Figure 3A,B. In these images, a nanosized CeO_2 (specific surface area of 63.7 m^2 g^{-1} and pore diameter of 12.4 nm) sample was also included for comparison purposes. The description of the synthesis method for CeO_2 is described elsewhere.[56] In the selected temperature range (50–400°C), all samples were able to completely oxidize CO before reaching the temperature of 350°C, using a 1:1 molar concentration of CO and O_2.

Figure 3A shows the catalytic activity for the samples calcined at 1200°C. It can be seen that by increasing the iron concentration, the temperature required to complete the reaction decreases, suggesting a dependence of the catalytic property on increasing the defects in the crystalline structure. The composition PZF10 1200 outperformed the CeO_2 sample and achieved 100% of CO conversion at 257°C.

The conversion curves of the samples calcined at 1400°C (Figure 3B) show the same tendency, where the catalytic activity improves with increasing iron concentration. The composition PZF10 1400 was also able to outperform the CeO_2 sample and completed the reaction at 264°C.

On comparing the different calcination temperatures, the samples calcined at 1200°C show slightly better catalytic activity. As the compositions that contain the highest concentration of iron are the ones with the highest

TABLE 2 CO conversion temperatures and activation energy of the prepared compositions compared to a CeO_2 sample

Reference	T50% conv. (°C)	T90% conv. (°C)	T90%–T50% (°C)	Activation energy (kJ mol^{-1})
PZ0 1200	326.8	340.3	13.5	101.2
PZF05 1200	275.3	287.2	11.9	92.0
PZF10 1200	243.6	255.4	11.7	84.4
PZ0 1400	326.7	339.1	12.4	123.0
PZF05 1400	292.3	302.8	10.5	128.0
PZF10 1400	251.1	261.2	10.1	85.3
CeO_2	251.5	272.2	20.7	51.3

catalytic activity, the surface area and the particle size are not determining factors in this catalytic process. This evidence can be seen in Figure 3C,D, where the rate of CO oxidation is normalized by the specific surface areas obtained by BET. On considering the surface area of each sample, it can be observed that the compositions that present the highest rate of CO oxidation are the ones with the highest Fe concentration. Moreover, due to the low surface area, the samples calcined at 1400°C present higher oxidation rates than both the samples calcined at 1200°C and the CeO_2 sample.

Another interesting aspect is the temperature range of the conversion curves. Although the conversion curve of the CeO_2 sample is wider, where the reaction starts at around 150°C and ends at 275°C, the samples of the $Pr_2Zr_{2-x}Fe_xO_{7\pm\delta}$ system present a shorter conversion temperature range as the iron concentration increases, as can be seen in Table 2. The data presented in the table show the temperature at which the system reaches 50% and 90% of CO conversion. All the compositions, calcined at both 1200 and 1400°C, show a smaller temperature interval between these two conversion stages compared to the curve of CeO_2. This behavior may be associated with the ability of the material to undergo reduction in a shorter temperature range by increasing the amount of Fe. On examining the values of activation energy calculated and shown in this table, the ceria sample presents lower activation energy (51.3 kJ mol^{-1}) than the pyrochlores, and for the compositions that were prepared, the ones that present lower activation energy are the samples with higher iron concentration, with calculated values of 84.4 and 85.3 kJ mol^{-1} for the PZF10 1200 and PZF10 1400 samples, respectively.

To verify possible changes in the oxidation state of praseodymium and iron, as well as to understand the role of oxygen absorption during the conversion reaction, the PZ0 and PZF10 samples fired at 1200°C were analyzed by XPS before and after the CO oxidation reaction. The peak deconvolution details are described in Tables S2 and S3 for

the PZ0 1200 and PZF10 1200, respectively. All peaks were corrected according to the position of the adventitious C 1S peak located at 284.8 eV, as can be seen in Figure 4Sa,b. Figure 4A shows the XPS survey spectra depicting the presence of the expected elements.

Figure 4B,C shows the XPS spectra in the O 1s region for the PZ0 1200 and PZF10 1200 samples before and after the CO oxidation reaction, respectively. In Figure 4B before the reaction, three different peaks can be observed (O1, O2, and O3). The peak designated as O1 at ~533 eV is usually associated with the loosely bound surface oxygen species. The peak near 530 eV denoted as O2 is normally associated with surface lattice oxygen.[57,58] In addition, it is possible to notice a shoulder near 527 eV (O3) that may be associated with different interactions between Zr–O and Pr–O. The O3 peak can also be originated due to the interference of the concentration of oxygen vacancies in the material as demonstrated by Shirsath et al. for perovskites structures.[59,60]

After the CO oxidation reaction, an increase in the O1 peak can be noted, that is, after the reaction, there is a higher ratio between the amounts of oxygen absorbed compared to the oxygen present in the lattice. Thus, it is probable that the ability of the pyrochlore structure to absorb oxygen contributes to the catalysis process. There is also a slight decrease in the intensity of the O2 peak, which could be a sign of oxygen loss due to the reduction of Pr^{4+} species.

In Figure 4C, almost the same behavior is observed for the PZF10 1200 samples, but, in addition, a fourth peak (O4) is present at ~529 eV. As with the O2 and O3 peaks, it can be assumed that the appearance of this peak could be due to different interactions between the Pr–O, Zr–O, and Fe–O in the pyrochlore structure and the concentration of oxygen vacancies.

If the O1 peaks of both samples are compared before the reaction, it can be concluded that the PZF10 1200 sample shows less absorbed oxygen initially but can absorb a considerable amount of oxygen during the reaction (O1 $_{before\ reaction}$–O1 $_{after\ reaction}$). The percentage of the contribution of the peaks is described in Table 3.

Figure 4D shows the deconvolution for the PZF10 1200 sample before and after reaction in the Pr 3d region. The same procedure was followed for the PZ0 1200 sample. In this same figure, the peaks referring to the oxygen Auger peak (OKLL), and the Pr 3d$_{3/2}$ and Pr 3d$_{5/2}$ core levels were identified. The binding energy separation between the core levels is 20.4 eV, which is very close to that found for Pr_2O_3 reference spectra (20.7 eV),[61] indicating that the majority oxidation state in the PZF10 1200 sample is Pr^{3+}. The peak marked with c at ~928 eV is associated with Pr^{3+} due to the transition of electrons-d from the 3d^{10}4f^2 level to the Pr 4f states,[62] and the peak denoted as a' at ~966 eV is
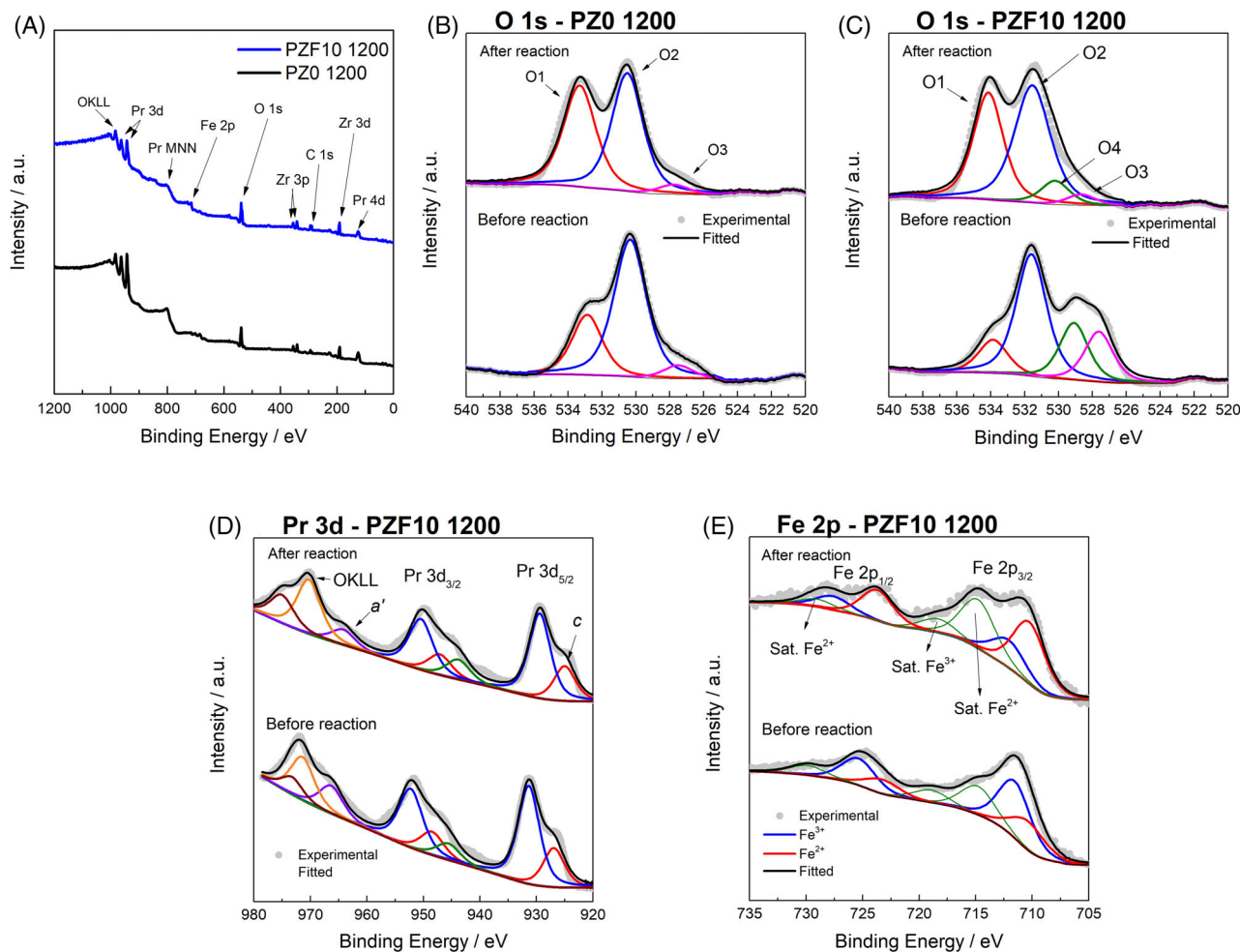
FIGURE 4 (A) Survey X-ray photoelectron spectroscopy (XPS) spectra and deconvolution of the (B and C) O 1s, (D) Pr 3d, and (E) Fe 2p regions for the PZ0 1200 and PZF10 1200 samples

TABLE 3 Peaks contribution (%) in the O 1s, Pr 3d, Fe 2p regions

		O 1s		Pr 3d			Fe 2p	
	Reference	$O_{surface}$ (O1)	$O_{lattice}$ (O2 + O3 + O4)	Peak a'	Peak c	a'/c	Fe^{3+}	Fe^{2+}
BR[a]	PZ0 1200	27.2	72.8	2.6	13.7	0.19		
	PZF10 1200	12.6	87.4	8.8	11.7	0.75	75.1	24.9
AR[a]	PZ0 1200	45.0	55.0	5.2	10.6	0.49		
	PZF10 1200	42.7	57.3	5.1	10.9	0.47	56.0	44.0

[a]Before reaction (BR) and after reaction (AR).

commonly associated with the presence of Pr^{4+}.[62,63] In this way, by comparing how each of these peaks are resolved, it is possible to estimate how the Pr^{4+}/Pr^{3+} (a'/c) ratio is changing. The values for the contribution of each peak are also shown in Table 3.

According to the a'/c ratio shown in Table 3, it is possible to estimate that the Fe-doped sample has a higher initial Pr^{4+} concentration than the PZ0 1200 sample (Figure 4Sc and Table S1). However, after the reaction, the ratio

between the peaks is almost the same, which may indicate that CO is able to reduce Pr^{4+} ions to Pr^{3+}, leading to an increase in the concentration of oxygen vacancies. This assumption is corroborated with the results observed in Figure 4B,C, because as a higher concentration of oxygen vacancies is expected in the PZF10 1200 sample, a higher oxygen absorption capacity is reasonable in this sample. The Kröger–Vink equation for the reduction of praseodymium is
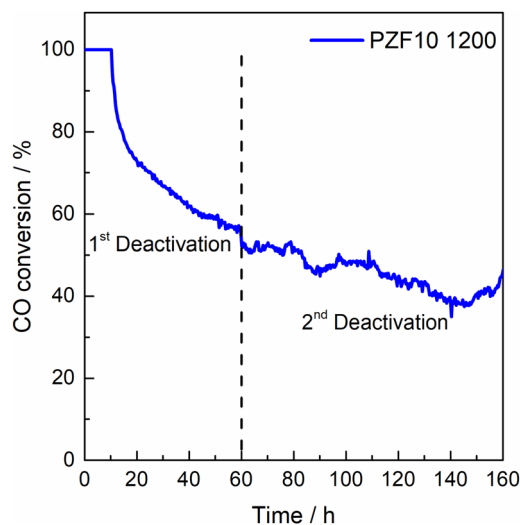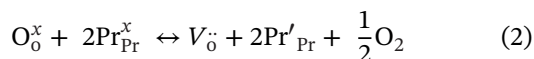
FIGURE 5 Long-term stability test of the PZF10 1200 sample for the CO oxidation reaction at 300°C

$$O_o^x + 2Pr_{Pr}^x \leftrightarrow V_o^{\cdot\cdot} + 2Pr'_{Pr} + \frac{1}{2}O_2 \qquad (2)$$

As shown in Figure 4E, the Fe $2p_{3/2}$ and Fe $2p_{1/2}$ core levels are located at around 710.6 and 724.2 eV, with a spin–orbit doublet splitting of 13.6 eV. In the Fe 2p spectrum, the Fe $2p_{3/2}$ and Fe $2p_{1/2}$ core levels can be resolved into two independent peaks, originating from Fe^{2+} and Fe^{3+} species, whereas Fe^{3+} has a higher binding energy than Fe^{2+}. Furthermore, one Fe^{3+} satellite peak at 718 eV and two satellite peaks of Fe^{2+} at close to 715 and 729 eV were assigned.[64,65] An analysis of the data in Table 3 shows that a large part of the Fe^{3+} species were reduced to Fe^{2+} during the reaction, which also generates a larger number of oxygen vacancies in the structure in a similar way to what occurs with praseodymium ions.

With the observed behavior of the CO oxidation reactions and the XPS data, a catalysis mechanism can be predicted for this system. During the catalysis reaction, where O_2 and CO are present, there is first a reduction of most of the Pr^{4+} and Fe^{3+} species, releasing O atoms that are captured by the CO molecules to generate CO_2. The reduction process also leads to the formation of oxygen vacancies, which will subsequently be occupied by O_2 molecules present in the atmosphere, thus starting a reaction cycle following a Mars–Van Krevelen mechanism.[66] Therefore, due to their capacity to absorb oxygen[48] and also the possible contribution of redox characteristics, the pyrochlore structures are able to catalyze the CO oxidation reaction.

To verify the stability of the composition that showed the best CO conversion, the PZF10 1200 sample was placed in the reactor at a temperature of 300°C, and it was left under the same flow conditions and gas concentrations as in the previous reactions. As shown in Figure 5, the sample exhibits a more accentuated deactivation in the rate of CO converted in the first 60 h and then practically stabilizes between 40% and 50% interval in the final 100 h.

The decrease in the conversion rate in the initial 60 h can possibly be explained by the reduction mainly of Pr^{4+} and Fe^{3+} species originated in the calcination process, which are unable to totally reoxidize at a temperature of 300°C. After this period, stabilization within a range of ~10% may be due to cyclic redox processes occurring in the material, where the constant O_2 absorption/release at the catalyst surface, as well as changes in the oxidation states of part of the species of praseodymium and iron, keep the catalytic activity more stable over a longer time interval.

4 | CONCLUSION

Using the solvothermal synthesis method, it was possible to obtain a single-phase pyrochlore structure for all nominal compositions with $x \leq 0.1$. The specific surface area calculated by the BET method and the particle size obtained by DLS showed a dependence of these two properties on increasing iron concentration and also on increasing calcination temperature. The SEM micrographs corroborated the BET and DLS results, where it is possible to notice a larger particle size with increasing iron concentration and signs of enhancement of the sintering process in the samples calcined at 1400°C, which together explain their smaller surface areas.

The materials proved to be efficient catalysts for the CO oxidation reaction, where all samples were able to convert 100% of CO to CO_2 at a temperature below 350°C. Moreover, by increasing the iron concentration, there was an increase in the conversion rate, and the PZF10 1200 and PZF10 1400 samples were the compositions that presented the best catalytic activity, completing the reaction at a lower temperature.

The XPS spectra in the O 1s region for the PZ0 1200 and PZF10 1200 samples show that after the CO conversion reaction, both samples contain a higher proportion of absorbed oxygen compared to the concentrations found before the reaction. This can be explained by the reduction of the Pr^{4+} and Fe^{3+} species, which leads to the formation of oxygen vacancies that can be occupied during the reaction. The reduction of these elements was also observed in the XPS spectra in the Pr 3d and Fe 2p region. Therefore, the main factors that contribute to the CO conversion, in this system, are the oxygen vacancies and the redox characteristics of the material.

ORCID

Emerson Luiz dos Santos Veiga https://orcid.org/0000-0001-6210-2481

Xavier Vendrell Villafruela https://orcid.org/0000-0003-4705-8253

Hector Beltrán-Mir https://orcid.org/0000-0002-7836-1602

REFERENCES

1. Nazir H, Batool M, Bolivar Osorio FJ, Isaza-Ruiz M, Xu X, Vignarooban K, et al. Recent developments in phase change materials for energy storage applications: a review. Int J Heat Mass Transfer [Internet]. 2019;129:491–523. Available from: https://doi.org/10.1016/j.ijheatmasstransfer.2018.09.126

2. Seh ZW, Kibsgaard J, Dickens CF, Chorkendorff I, Nørskov JK, Jaramillo TF. Combining theory and experiment in electrocatalysis: insights into materials design. Science (80–) [Internet]. 2017;355(6321):1–12. Available from: https://www.science.org/doi/10.1126/science.aad4998

3. Xu Y, Ramanathan V, Victor DG. Global warming will happen faster than we think. Nature [Internet]. 2018;564(7734):30–2. Available from: http://www.nature.com/articles/d41586-018-07586-5

4. Geiges A, Nauels A, Parra PY, Andrijevic M, Hare W, Pfleiderer P, et al. Incremental improvements of 2030 targets insufficient to achieve the Paris Agreement goals. Earth Syst Dyn [Internet]. 2020;11(3):697–708. Available from: https://esd.copernicus.org/articles/11/697/2020/

5. Watts N, Amann M, Arnell N, Ayeb-Karlsson S, Beagley J, Belesova K, et al. The 2020 report of The Lancet Countdown on health and climate change: responding to converging crises. Lancet. 2021;397(10269):129–70.

6. Landrigan PJ, Fuller R, Acosta NJR, Adeyi O, Arnold R, Basu NN, et al. The Lancet Commission on pollution and health. Lancet. 2018;391(10119):462–512.

7. Kim H-H, Choi S. Therapeutic aspects of carbon monoxide in cardiovascular disease. Int J Mol Sci [Internet]. 2018;19(8):2381. Available from: http://www.mdpi.com/1422-0067/19/8/2381

8. Dey S, Dhal GC. Materials progress in the control of CO and CO_2 emission at ambient conditions: an overview. Mater Sci Energy Technol [Internet]. 2019;2(3):607–23. Available from: https://doi.org/10.1016/j.mset.2019.06.004

9. Liu C, Yin P, Chen R, Meng X, Wang L, Niu Y, et al. Ambient carbon monoxide and cardiovascular mortality: a nationwide time-series analysis in 272 cities in China. Lancet Planet Health [Internet]. 2018;2(1):e12–8. Available from: https://doi.org/10.1016/S2542-5196(17)30181-X

10. Kampa M, Castanas E. Human health effects of air pollution. Environ Pollut [Internet]. 2008;151(2):362–7. Available from: https://linkinghub.elsevier.com/retrieve/pii/S0269749107002849

11. Manisalidis I, Stavropoulou E, Stavropoulos A, Bezirtzoglou E. Environmental and health impacts of air pollution: a review. Front Public Health [Internet]. 2020;8(February):1–13. Available from: https://www.frontiersin.org/article/10.3389/fpubh.2020.00014/full

12. He H, Wang HH, Liu J, Liu X, Li W, Wang Y. Research progress and application of single-atom catalysts: a review. Molecules [Internet]. 2021;26(21):6501. Available from: https://www.mdpi.com/1420-3049/26/21/6501

13. Tang S, Xu L, Peng B, Xiong F, Chen T, Luo X, et al. Ga-doped Pd/CeO model catalysts for CO oxidation reactivity: a density functional theory study. Appl Surf Sci [Internet]. 2022;575:151655. Available from: https://doi.org/10.1016/j.apsusc.2021.151655

14. Xiang G, Zhao S, Wei C, Liu C, Fei H, Liu Z, et al. Atomically dispersed Au catalysts for preferential oxidation of CO in H_2-rich stream. Appl Catal B Environ [Internet]. 2021;296(May):120385. Available from: https://doi.org/10.1016/j.apcatb.2021.120385

15. Gan T, He Q, Zhang H, Xiao H, Liu Y, Zhang Y, et al. Unveiling the kilogram-scale gold single-atom catalysts via ball milling for preferential oxidation of CO in excess hydrogen. Chem Eng J [Internet]. 2020;389:124490. Available from: https://doi.org/10.1016/j.cej.2020.124490

16. Zhang H, Fang S, Hu YH. Recent advances in single-atom catalysts for CO oxidation. Catal Rev [Internet]. 2022;64(3):491–532. Available from: https://doi.org/10.1080/01614940.2020.1821443

17. Zhao S, Lin J, Wu P, Ye C, Li Y, Li A, et al. A hydrothermally stable single-atom catalyst of Pt supported on high-entropy oxide/Al_2O_3: structural optimization and enhanced catalytic activity. ACS Appl Mater Interfaces [Internet]. 2021;13(41):48764–73. Available from: https://pubs.acs.org/doi/10.1021/acsami.1c14456

18. Chen Y, Ji S, Chen C, Peng Q, Wang D, Li Y. Single-atom catalysts: synthetic strategies and electrochemical applications. Joule [Internet]. 2018;2(7):1242–64. Available from: https://doi.org/10.1016/j.joule.2018.06.019

19. Liu L, Corma A. Metal catalysts for heterogeneous catalysis: from single atoms to nanoclusters and nanoparticles. Chem Rev [Internet]. 2018;118(10):4981–5079. Available from: https://pubs.acs.org/doi/10.1021/acs.chemrev.7b00776

20. Zhou G-F, Ma J, Bai S, Wang L, Guo Y. CO catalytic oxidation over Pd/CeO_2 with different chemical states of Pd. Rare Met [Internet]. 2020;39(7):800–5. Available from: https://doi.org/10.1007/s12598-019-01347-7

21. Venkataswamy P, Damma D, Jampaiah D, Mukherjee D, Vithal M, Reddy BM. Cr-doped CeO_2 nanorods for CO oxidation: insights into promotional effect of Cr on structure and catalytic performance. Catal Lett [Internet]. 2020;150(4):948–62. Available from: https://doi.org/10.1007/s10562-019-03014-z

22. Qi F, Zhang J, Song L, Niu S, Yang Z, Wang Y, et al. Engineering dual active sites at the interface between nanoporous Pt and nanosized CeO₂ to enhance photo-thermocatalytic CO Oxidation. Adv Mater Interfaces [Internet]. 2021;8(14):2100581. Available from: https://onlinelibrary.wiley.com/doi/10.1002/admi.202100581

23. Rao R, Shao F, Dong X, Dong H, Fang S, Sun H, et al. Effect of Ag-CeO₂ interface formation during one-spot synthesis of Ag-CeO₂ composites to improve their catalytic performance for CO oxidation. Appl Surf Sci [Internet]. 2020;513(February):145771. Available from: https://linkinghub.elsevier.com/retrieve/pii/S0169433220305274

24. Ge C, Sun J, Tong Q, Zou W, Li L, Dong L. Synergistic effects of CeO₂/Cu₂O on CO catalytic oxidation: electronic interaction and oxygen defect. J Rare Earths [Internet]. 2022;40(8):1211–8. Available from: https://linkinghub.elsevier.com/retrieve/pii/S100207212100199X

25. Papadopoulos C, Kappis K, Papavasiliou J, Vakros J, Kuśmierz M, Gac W, et al. Copper-promoted ceria catalysts for CO oxidation reaction. Catal Today [Internet]. 2020;355:647–53. Available from: https://doi.org/10.1016/j.cattod.2019.06.078

26. Laguna OH, Centeno MA, Romero-Sarria F, Odriozola JA. Oxidation of CO over gold supported on Zn-modified ceria catalysts. Catal Today [Internet]. 2011;172(1):118–23. Available from: http://doi.org/10.1016/j.cattod.2011.02.015

27. Li Y, Gan L, Si R. Effect of tungsten oxide on ceria nanorods to support copper species as CO oxidation catalysts. J Rare Earths [Internet]. 2021;39(1):43–50. Available from: https://doi.org/10.1016/j.jre.2019.12.015

28. Kim HJ, Shin D, Jeong H, Jang MG, Lee H, Han JW. Design of an ultrastable and highly active ceria catalyst for CO oxidation by rare-earth- and transition-metal Co-doping. ACS Catal [Internet]. 2020;10(24):14877–86. Available from: https://pubs.acs.org/doi/10.1021/acscatal.0c03386

29. Rejith RS, Solomon S. Influence of pyrochlore domains on the structure and electrical properties Gd₂₋ₓDyₓZr₁.₅Hf₀.₅O₇ energy materials. J Alloys Compd [Internet]. 2021;855:157291. Available from: https://linkinghub.elsevier.com/retrieve/pii/S0925838820336550

30. Anantharaman AP, Dasari HP. Potential of pyrochlore structure materials in solid oxide fuel cell applications. Ceram Int [Internet]. 2021;47(4):4367–88. Available from: https://doi.org/10.1016/j.ceramint.2020.10.012

31. Cao J, Su C, Ji Y, Yang G, Shao Z. Recent advances and perspectives of fluorite and perovskite-based dual-ion conducting solid oxide fuel cells. J Energy Chem [Internet]. 2021;57:406–27. Available from: https://linkinghub.elsevier.com/retrieve/pii/S2095495620306422

32. Su H, Hu YH. Progress in low-temperature solid oxide fuel cells with hydrocarbon fuels. Chem Eng J [Internet]. 2020;402:126235. Available from: https://linkinghub.elsevier.com/retrieve/pii/S1385894720323639

33. Weng S-F, Hsieh H-C, Lee C-S. Hydrogen production from oxidative steam reforming of ethanol on nickel-substituted pyrochlore phase catalysts. Int J Hydrogen Energy [Internet]. 2017;42(5):2849–60. Available from: https://linkinghub.elsevier.com/retrieve/pii/S0360319916335145

34. Zhong F, Shi L, Zhao J, Cai G, Zheng Y, Xiao Y, et al. Ce incorporated pyrochlore Pr₂Zr₂O₇ solid electrolytes for enhanced mild-temperature NO₂ sensing. Ceram Int [Internet]. 2017;43(15):11799–806. Available from: http://doi.org/10.1016/j.ceramint.2017.06.019

35. Zhong F, Zhao J, Shi L, Cai G, Zheng Y, Zheng Y, et al. Pyrochlore Pr₂Zr₁.₉₅In₀.₀₅O₇₊δ oxygen conductors:defect-induced electron transport and enhanced NO₂ sensing performances. Electrochim Acta [Internet]. 2019;293:338–47. Available from: https://doi.org/10.1016/j.electacta.2018.09.152

36. Yang Z, Zhang P, Pan W, Han Y, Huang M, Chen H, et al. Thermal and oxygen transport properties of complex pyrochlore RE₂InTaO₇ for thermal barrier coating applications. J Eur Ceram Soc [Internet]. 2020;40(15):6229–35. Available from: https://doi.org/10.1016/j.jeurceramsoc.2020.06.027

37. Che J, Wang X, Liu X, Liang G, Zhang S. Outstanding sintering resistance in pyrochlore-type La₂(Zr₀.₇Ce₀.₃)₂O₇ for thermal barrier coatings material. Ceram Int. [Internet]. 2020;47(5):6996–7004. Available from: https://doi.org/10.1016/j.ceramint.2020.11.050

38. Kaviyarasu K, Maria Magdalane C, Jayakumar D, Samson Y, Bashir AKH, Maaza M, et al. High performance of pyrochlore like Sm₂Ti₂O₇ heterojunction photocatalyst for efficient degradation of rhodamine-B dye with waste water under visible light irradiation. J King Saud Univ – Sci [Internet]. 2020;32(2):1516–22. Available from: https://doi.org/10.1016/j.jksus.2019.12.006

39. Wang B, Wang Z, Ai L, Liu W, Li Q, Wang X, et al. High performance of K-supported Pr₂Sn₂O₇ pyrochlore catalysts for soot oxidation. Fuel [Internet]. 2022;317(2):123467. Available from: https://doi.org/10.1016/j.fuel.2022.123467

40. Kong X, Li Z, Shao Y, Ren X, Li K, Wu H, et al. Modulate the superficial structure of La₂Ce₂O₇ catalyst with anchoring CuO species for the selective catalytic oxidation of NH₃. J Mater Sci Technol [Internet]. 2022;111:1–8. Available from: https://doi.org/10.1016/j.jmst.2021.09.044

41. Bai J, Fu Y, Kong W, Pan B, Yuan C, Li S, et al. Design of Ni-substituted La₂(CeZrNi)₂O₇ pyrochlore catalysts for methane dry reforming. ChemNanoMat [Internet]. 2022;8(3):e202100422. Available from: https://onlinelibrary.wiley.com/doi/10.1002/cnma.202100422

42. Burnett DL, Petrucco E, Kashtiban RJ, Parker SF, Sharman JDB, Walton RI. Exploiting the flexibility of the pyrochlore composition for acid-resilient iridium oxide electrocatalysts in proton exchange membranes. J Mater Chem A [Internet]. 2021;9(44):25114–27. Available from: http://xlink.rsc.org/?DOI=D1TA05457K

43. Han T, Wu J, Lu X, Wang Y, Zhao H, Tang X. Study of OER electrocatalysts performance of Fe/Mn doped pyrochlore structure. J Solid State Chem [Internet]. 2021;303(July):122457. Available from: https://doi.org/10.1016/j.jssc.2021.122457

44. Jayaraman V, Ayappan C, Vattikondala G, Mani A. Preparation and characterization of the Cu, Fe co-doped Bi₂Ti₂O₇/EG-g-C₃N₄ material for organic model pollutants removal under direct sun light irradiation. Mater Res Bull [Internet]. 2021;143(March):111439. Available from: https://doi.org/10.1016/j.materresbull.2021.111439

45. Xu J, Xi R, Xu X, Zhang Y, Feng X, Fang X, et al. A₂B₂O₇ pyrochlore compounds: a category of potential materials for clean energy and environment protection catalysis. J Rare Earths [Internet]. 2020;38(8):840–9. Available from: https://doi.org/10.1016/j.jre.2020.01.002

46. Zhao J, Liu Y, Fan Y, Zhang W, Zhang C, Yang G, et al. Native point defects and oxygen migration of rare earth zirconate and stannate pyrochlores. J Mater Sci Technol [Internet]. 2021;73:23–30. Available from: https://doi.org/10.1016/j.jmst.2020.09.033

47. Redkin AF, Ionov AM, Nekrasov AN, Mozhchil RN, Reutova OV. Structural aspects of pyrochlores stability: influence of the cations in 8A, 6B positions and lattice parameters. Phys Chem Miner [Internet]. 2020;47(11):47. Available from: https://doi.org/10.1007/s00269-020-01114-6

48. Veiga EL dos S, Fortuño-Morte M, Beltrán-Mir H, Cordoncillo E. Effect of the oxidation states on the electrical properties of Fe-doped $Pr_2Zr_2O_7$ pyrochlore. J Mater Res Technol [Internet]. 2022;16:201–15. Available from: https://linkinghub.elsevier.com/retrieve/pii/S2238785421014253

49. Shirsath SE, Wang D, Jadhav SS, Mane ML, Li S. Ferrites obtained by sol–gel method. In: Handbook of sol-gel science and technology [Internet]. Cham: Springer International Publishing; 2018. p. 1–41. Available from: http://link.springer.com/10.1007/978-3-319-19454-7_125-3

50. Wuensch B. Connection between oxygen-ion conductivity of pyrochlore fuel-cell materials and structural change with composition and temperature. Solid State Ionics [Internet]. 2000;129(1–4):111–33. Available from: https://linkinghub.elsevier.com/retrieve/pii/S0167273899003203

51. Vasundhara K, Achary SN, Tyagi AK. Structure, thermal and electrical properties of calcium doped pyrochlore type praseodymium zirconate. Int J Hydrogen Energy [Internet]. 2015;40(11):4252–62. Available from: http://doi.org/10.1016/j.ijhydene.2015.01.148

52. Shannon RD. Revised effective ionic radii and systematic studies of interatomic distances in halides and chalcogenides. Acta Crystallogr Sect A [Internet]. 1976;32(5):751–67. Available from: http://scripts.iucr.org/cgi-bin/paper?S0567739476001551

53. Lankauf K, Mroziński A, Błaszczak P, Górnicka K, Ignaczak J, Łapiński M, et al. The effect of Fe on chemical stability and oxygen evolution performance of high surface area $SrTi_{x-1}Fe_xO_{3-\delta}$ mixed ionic-electronic conductors in alkaline media. Int J Hydrogen Energy [Internet]. 2021;46(56):28575–90. Available from: https://linkinghub.elsevier.com/retrieve/pii/S0360319921022394

54. Ilić S, Babić B, Bjelajac A, Stoimenov N, Kljajević L, Pošarac-Marković M, et al. Structural and morphological characterization of iron-doped sol-gel derived mullite powders. Ceram Int [Internet]. 2020;46(9):13107–13. Available from: https://linkinghub.elsevier.com/retrieve/pii/S0272884220304053

55. Mays TJ. A new classification of pore sizes. In: Studies in surface science and catalysis [Internet]. The Netherlands: Elsevier; 2007. p. 57–62. Available from: https://linkinghub.elsevier.com/retrieve/pii/S0167299107800097

56. Vendrell X, Kubyshin Y, Mestres L, Llorca J. CO oxidation on ceria studied by electrochemical impedance spectroscopy. ChemCatChem. 2020;12(23):5926–31.

57. Zhang X, Fang X, Feng X, Li X, Liu W, Xu X, et al. $Ni/Ln_2Zr_2O_7$ (Ln = La, Pr, Sm and Y) catalysts for methane steam reforming: the effects of A site replacement. Catal Sci Technol [Internet]. 2017;7(13):2729–43. Available from: http://xlink.rsc.org/?DOI=C7CY00004A

58. Shlyakhtina A, Knotko A, Boguslavskii M, Stefanovich S, Kolbanev I, Larina L, et al. Effect of non-stoichiometry and synthesis temperature on the structure and conductivity of $Ln_{2+x}M_{2-x}O_{7-x/2}$ (Ln = Sm–Gd; M = Zr, Hf; x = 0–0.286). Solid State Ionics [Internet]2007;178(1–2):59–66. Available from: https://linkinghub.elsevier.com/retrieve/pii/S0167273806006539

59. Shirsath SE, Assadi MHN, Zhang J, Kumar N, Gaikwad AS, Yang J, et al. Interface-driven multiferroicity in Cubic $BaTiO_3$-$SrTiO_3$ nanocomposites. ACS Nano [Internet]. 2022;16:15416–24. Available from: https://pubs.acs.org/doi/10.1021/acsnano.2c07215

60. Shirsath SE, Liu X, Yasukawa Y, Li S, Morisako A. Switching of magnetic easy-axis using crystal orientation for large perpendicular coercivity in $CoFe_2O_4$ thin film. Sci Rep [Internet]. 2016;6(1):30074. Available from: https://doi.org/10.1038/srep30074

61. Mekki A, Ziq KA, Holland D, McConville CF. Magnetic properties of praseodymium ions in Na_2O-Pr_2O_3-SiO_2 glasses. J Magn Magn Mater. 2003;260(1–2):60–9.

62. Tankov I, Pawelec B, Arishtirova K, Damyanova S. Structure and surface properties of praseodymium modified alumina. Appl Surf Sci [Internet]. 2011;258(1):278–84. Available from: http://doi.org/10.1016/j.apsusc.2011.08.046

63. Shlyakhtina AV, Abrantes JCC, Gomes E, Shchegolikhin AN, Vorobieva GA, Maslakov KI, et al. Effect of Pr^{3+}/Pr^{4+} ratio on the oxygen ion transport and thermomechanical properties of the pyrochlore and fluorite phases in the ZrO_2-Pr_2O_3 system. Int J Hydrogen Energy [Internet]. 2016;41(23):9982–92. Available from: http://doi.org/10.1016/j.ijhydene.2016.02.152

64. Li Y, Sritharan T, Zhang S, He X, Liu Y, Chen T. Multiferroic properties of sputtered $BiFeO_3$ thin films. Appl Phys Lett. 2008;92(13):13–6.

65. Yamashita T, Hayes P. Analysis of XPS spectra of Fe^{2+} and Fe^{3+} ions in oxide materials. Appl Surf Sci [Internet]. 2008;254(8):2441–9. Available from: https://linkinghub.elsevier.com/retrieve/pii/S0169433207013748

66. Aneggi E, Llorca J, Boaro M, Trovarelli A. Surface-structure sensitivity of CO oxidation over polycrystalline ceria powders. J Catal [Internet]. 2005;234(1):88–95. Available from: https://linkinghub.elsevier.com/retrieve/pii/S0021951705002435

SUPPORTING INFORMATION

Additional supporting information can be found online in the Supporting Information section at the end of this article.